Machine Vision and Applications (2003) 13: 352–362
Digital Object Identifier (DOI) 10.1007/s00138-002-0087-9

Machine Vision and Applications
© Springer-Verlag 2003

Fractal analysis of tumor in brain MR images

Khan M. Iftekharuddin[1], **Wei Jia**[2], **Ronald Marsh**[3]

[1] Department of Electrical and Computer Engineering, The University of Memphis, Memphis, TN 38152, USA; e-mail: iftekhar@memphis.edu
[2] Department of Computer Science, North Dakota State University, Fargo, ND 58105, USA
[3] Department of Computer Science, University of North Dakota, Grand Forks, ND 58202, USA

Received: 13 October 2001 / Accepted: 28 May 2002

Abstract. The purpose of this study is to discuss existing fractal-based algorithms and propose novel improvements of these algorithms to identify tumors in brain magnetic-response (MR) images. Considerable research has been pursued on fractal geometry in various aspects of image analysis and pattern recognition. Magnetic-resonance images typically have a degree of noise and randomness associated with the natural random nature of structure. Thus, fractal analysis is appropriate for MR image analysis. For tumor detection, we describe existing fractal-based techniques and propose three modified algorithms using fractal analysis models. For each new method, the brain MR images are divided into a number of pieces. The first method involves thresholding the pixel intensity values; hence, we call the technique piecewise-threshold-box-counting (PTBC) method. For the subsequent methods, the intensity is treated as the third dimension. We implement the improved piecewise-modified-box-counting (PMBC) and piecewise-triangular-prism-surface-area (PTPSA) methods, respectively. With the PTBC method, we find the differences in intensity histogram and fractal dimension between normal and tumor images. Using the PMBC and PTPSA methods, we may detect and locate the tumor in the brain MR images more accurately. Thus, the novel techniques proposed herein offer satisfactory tumor identification.

Key words: MRI – Brain tumor – Fractal dimension – Cumulative histogram – Image recognition

1. Introduction

The fractal concept developed by Mandelbrot [1], who coined the term "fractal" from the Latin "fractus," provides a useful tool for explaining a variety of naturally occurring phenomena. A fractal is an irregular geometric object with an infinite nesting of structure at all scales. Fractal objects can be found everywhere in nature, such as in coastlines, fern trees, snow flakes, clouds, mountains, and bacteria. Some of the most important properties of fractals are self-similarity, chaos, and non-integer fractal dimension (FD). Fractals are self-similar, which means that structures are repeated at different scales of size. The fractal dimension gives a quantitative measure of self-similarity and scaling.

A considerable number of applications using fractal geometry have been studied in many areas in the past. The FD analysis of objects has been applied in various application areas. The FD analysis method has been successful in identifying corn roots stressed by nitrogen fertilizer [2], steer body temperature fluctuations in hot and cool chambers [2], measuring textural images [3] and surface roughness [3]. Medical images typically have a degree of randomness associated with the natural random nature of structure. The fractal model has also been proved to be useful in analyzing a wide variety of medical images. The effects of system noise and modulation-transfer function on FD were explored to measure of structural bone strength using a hand phantom [5]. Osman et al. [6] analyzed FD of trabecular bone to evaluate its potential structure. Other studies successfully used FD to detect microcalcifications in mammograms [7], predict osseous changes in ankle fractures [8], diagnose small peripheral lung tumors [9], and distinguish breast tumors in digitized mammograms [10]. The studies have also shown that the changes in the fractal dimension value reflect alterations of structural properties.

Brain magnetic resonance images (MRI) are candidates for characterization using fractal analysis because of their highly complex structure [11]. Bru et al. [12] analyzed the cultivated typical brain-tumor contour cell FD dynamically and morphologically. Penn et al. [13] used a one-dimensional box-counting method to measure the contour of the tumor cell. The user specifies a rectangular region of interest (ROI) around the mass and the algorithm generates a segmentation zone from the ROI. Fractal models are constructed on multiple-threshold-intensity contours within the segmentation zone. In this research, we propose three new FD analysis algorithms: piecewise-threshold box-counting (PTBC), piecewise-modified box-counting (PMBC), and piecewise-triangular-prism surface-area (PTPSA) to detect tumors in brain MR images based in two- and three-dimensional spaces.

Correspondence to: K.M. Iftekharuddin

2. Background on fractal geometry

2.1. Concept of fractal

Euclidean geometry describes points, lines, planes, and cubes. Euclidean objects are composed of an integer dimension. It is known that a line has the dimension of one because there is only one way to move on a line. Two-dimensional figures like squares or circles have two directions in which to move, and three-dimensional objects like cubes have three directions to move. Mandelbrot [1] used the term "topological dimension" to describe these shapes. The Euclidean dimensions may not adequately describe the morphology and behavior of the complex objects and relationships that are found in nature. The fractal theory developed by Mandelbrot is based, in part, on the work of mathematicians Hausdorff and Besicovitch [14]. The Hausdorff–Besicovitch dimension, D_H is defined as:

$$D_H = \lim_{r \to 0^+} \frac{\ln N}{\ln 1/r}, \tag{1}$$

where N is the number of elements of the box size, r, required to form a cover of the object. Mandelbrot [1] defines a fractal as a set for which the Hausdorff–Besicovich dimension strictly exceeds the topological dimension. Fractals are used to characterize, explain, and model complex objects in nature and artificial objects [1]. Fractal geometry describes objects in non-integer dimension. While a straight line has a dimension of exactly one, a fractal curve (e.g., a Koch curve or a Sierpinski triangle) may have a dimension between one and two. All fractal objects share the following three characteristics [1]:

a. Self-resemblance: When the fractal objects are observed closely, their self-similar nature becomes obvious. Self-similar means that any portion of the object would appear identical to the whole object.
b. Chaotic and very complex: The apparent unpredictable behavior of fractal is due to its sensitivity to initial conditions.
c. Non-integer fractal dimension: The property of fractal self-similarity can be measured quantitatively with fractal dimension.

2.2. Fractal dimension

The fractal dimension can be defined as the exponent of the number of self-similar pieces, N, with magnification factor, $1/r$, into which a figure may be broken. The equation for FD is as follows:

$$FD = \frac{\ln \text{ (number of self-similar pieces)}}{\ln \text{ (magnification factor)}} = \frac{\ln N}{\ln(1/r)} \tag{2}$$

The FD is a non-integer value in contrast to objects that lie strictly in Euclidean space. A fractal curve has a fractal dimension between a straight line and a plane $(1 < FD < 2)$, while a fractal surface has a dimension between a plane and three-dimensional space $(2 < FD < 3)$. The fractal dimension characterizes an object with a dimensionality greater than its topographical dimension.

2.2.1. Fractal dimension measurement

Hausdorff [14] suggests one way to generalize the notion of dimension. The idea of generalization involves measuring the same object with different units of measurement. The measure is called the topological dimension of a space. A topological property of an entity is one that remains invariant under continuous one-to-one transformations. Throughout such processes, the topological dimension does not change. A line segment has a topological dimension of one. In each step, we reduce the image size by r in each spatial direction, thus, its measure will increase to $N = (1/r)^D$ times the original, where r is the magnification factor, N is the number of self-similar pieces, and FD is the fractal dimension as given in Eq. 1.

2.2.2. Methods of estimating fractal dimension

The concept of self-similarity can be used to estimate the FD. There are a wide variety of computer algorithms [1, 3, 13] for estimating the FD of a structure, such as the box-counting (BC), modified-box-counting (MBC), fractional-Brownian-motion, and triangular-prism-surface-area methods. The algorithm for box counting estimates how many boxes are taken up by the fractal structure. An arbitrary grid is placed over the structure to be measured, and the number of boxes in the grid that are filled by the fractal structure is counted.

Box-counting method
The box-counting principle [1] is based on counting the number of boxes having side length r needed to cover the surface of a fractal object and the number of grid boxes, N, occupied by one or more pixels of the image. Thus, the box-counting procedure is mainly defined by two parameters: the selection of r and the range of r. Since a digitized image consists of a finite set of points, we have an upper limit (image size) and lower limit (pixel unit). The box size and the number of boxes counted can only be an integer. Some research [13] recommends using $2, 4, 8, 16, \ldots, 2^n$ pixels as box sizes, r, to give a uniform spread of observations on the independent variable during the log-log least square regression. The FD of the fractal object is estimated by the slope of points ($\log N$ versus $\log 1/r$), which normally lies on a straight line.

Modified box-counting method for measuring surface fractal dimension
The BC approach is suitable for one-dimensional fractal calculation for objects, such as Koch curves, coastlines, and even speech-wave graphs. However, the BC method may not be suitable for two-dimensional images, such as clouds, rugged surfaces, and medical images. A different method, namely, modified box counting is proposed by Sarkar et al. [3] to estimate fractal dimension in rough images. In this method, the image of size $M \times M$ pixels is scaled down to a size $r \times r$, where $M/2 \geq r > 1$ and r is an integer. Consider the image $i(x, y)$ as a two-dimensional plane and the pixel intensity r' as the height above a plane. Then the intensity surface of the image can be viewed as a rugged surface, as shown in Fig. 1. Thus, image $i(x, y)$ is partitioned into grids of size $r \times r$, and on each grid there is a column of boxes of size $r \times r \times r'$. Figure 1 shows that $r = r' = 3$. Assume that the maximum and minimum gray levels of the image $i(x, y)$ in (i, j)th grid fall in box numbers k and l, respectively. Then $n_r(i, j) = k - l + 1$

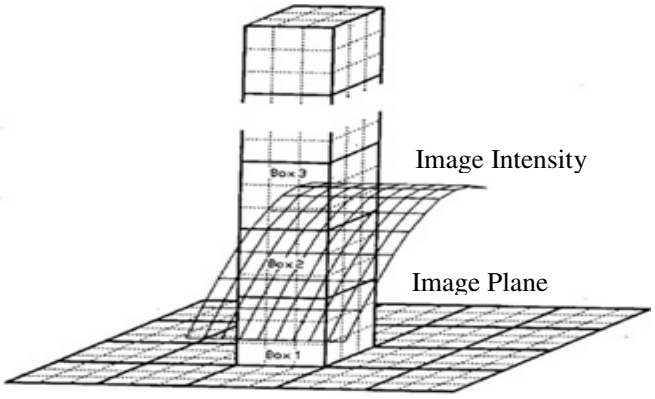

Fig. 1. Determination of N_r for modified box-counting method [3]

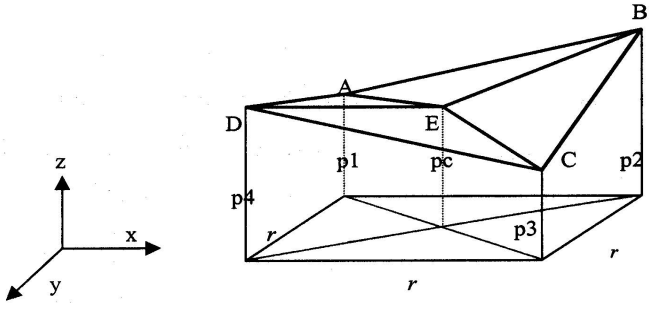

Fig. 2. Triangular-prism-surface-area method. The $p1, p2, p3$, and $p4$ are the grayscale elevation values at box corner, pc is the average of corner values. ABE, BCE, CDE, and DAE are four triangles

is the contribution of N_r in the (i, j)th grid. The contribution of N_r in Fig. 1 is $n_r(i, j) = 3 - 1 + 1$. The contributions from all the grids using the equation

$$N_r = \sum_{i,j} n_r(i, j), \tag{3}$$

where $N_r$is computed for different values of the square of size r. The FD of an image is calculated from the slope of the linear regression line obtained when the horizontal axis, and the vertical axis are taken as $\log 1/r$ and $\log N_r$. Sarkar et al. [3] indicates that this method offers a better approximation to the boxes intersecting the image-intensity surface. The basic box-counting method does not cover the image surface as well and, hence, cannot capture the fractal dimension for a rough-textured surface.

Triangular-prism-surface-area procedure

The triangular-prism-surface-area (TPSA) method is proposed by Clarke [15]. The method uses the grayscale elevation values at the corners of a box $(p1, p2, p3,$ and $p4)$, and the average value of the corners as center elevation value (pc) forms four triangles (ABE, BCE, CDE, and DAE), as shown in Fig. 2. By repeating this calculation for different box sizes, r, the logarithms of surface areas of the top triangular surfaces versus the logarithms of the box sizes is calculated to obtain the slope (FD).

Fractional-Brownian-motion model

As described by Mandelbrot and Van Ness [16], fractional-Brownian-motion (FBM) is a statistically self-affine fractal, which is an extension of the concept of Brownian motion. Fractional Brownian motion regards rough surfaces as the result of random walks. An intensity surface of medical images may also be viewed as the end result of a random walk. The fractional-Brownian-motion model may be used for the analysis of medical images. Mandelbrot and Van Ness [16] define the FBM as nonstationary self-affine random process given by the equation

$$\begin{aligned} &B_H(t,\omega) - B_H(0,\omega) \\ &= \frac{1}{\Gamma(H+\frac{1}{2})}\left\{\int_{-\infty}^{0}[(t-s)^{(H-1/2)} \right. \\ &\quad -(-s)^{(H-1/2)}]dB_H(s,\omega) \\ &\quad \left. + \int_0^t (t-s)^{(H-1/2)} dB_H(s,\omega)\right\}, \end{aligned} \tag{4}$$

where B_H is reduced fractional Brownian motion, H is self-similar parameter in the range $0 < H < 1, t$ is time $(-\infty < t < \infty)$, and ω is the experimental outcome. When H is 0, FBM is a well-known Brownian motion process. The Hurst coefficient H quantifies the roughness of the curves $B_H(t, \omega)$. The curve $B_H(t, \omega)$ is very rough if $H = 0.01$, while for $H = 0.99$, the curve is very smooth. The fractal dimension is related to the Hurst coefficient H by the equation,

$$D = E + 1 - H. \tag{5}$$

The parameter $E + 1$ is the Euclidean dimension of the space of the fractal.

2.2.3. Example: One-dimensional FD calculation

We consider the fractal geometry for a Koch curve to demonstrate the BC algorithm. We use box sizes, r, of $13, 11, 9, 7, 5,$ and 3 pixels, respectively, to map onto the Koch curve. The corresponding occupied box numbers, N, are $54, 65, 88, 137, 196,$ and 319, respectively. A linear regression of the $\log N$ versus $\log 1/r$ yields the slope (FD) of 1.244 and correlation coefficient of 0.993, respectively. The estimated error of the fractal dimension is 1.37%. The high value of the correlation coefficient indicates good linear fit of the data. For the next example, we use box sizes, r, of $13, 11, 9, 7, 5,$ and 3 pixels, respectively, to map onto the Sierpinski triangle. The corresponding occupied box numbers, N, are $69, 94, 142, 188, 326,$ and 711, respectively. A linear regression of the $\log N$ versus $\log 1/r$ yields the FD of 1.565, and correlation coefficient of 0.998, respectively. The estimated error of the fractal dimension is 1.26%. Thus, the acceptable accuracy of the box-counting method motivates us to use BC as the basis model for subsequent development of PTBC, PMBC, and PTPSA methods, respectively.

3. Fractal dimension algorithms

3.1. System environment

The fractal image-analysis program is developed in C on a Unix operating system. The program possesses a high degree of portability to various platforms. The source code may be

complied with the GNU gcc-compiler. The fractal image analysis is done either on entire image or on a selected portion of the image. The digitized image is first scanned from left to right, and from top to bottom to find the count number (N) in the response box size (r). The box sizes in this program are $3, 5, 7, 9, 11$, and 13 pixels, respectively. The FD is estimated using a least-square-regression method to find the straight line that is fitted to the points of $\log N$ versus $\log 1/r$.

3.2. Algorithm flow charts

For fractal image analysis of MR brain images, we propose three different algorithms. For these methods, the brain MR images are divided into a number of pieces. The first method involves thresholding the pixel intensity values, and hence, we call the technique the piecewise-threshold-box-counting method. In the second and third methods, the intensity is treated as the third dimension. We then proceed to implement the improved piecewise-modified-box-counting and piecewise-triangular-prism-surface-area methods, respectively. Before describing the details of the algorithms, we first explain the key step that is common to all procedures. The first step in all three algorithms is to divide the image into a number of pieces.

In general, a tumor only occupies a small portion in the MR image. Hence, a tumor in the MR brain image may be detected and located more accurately if the image is divided into small pieces. The size of two images, such as grayscale cloud and MR brain images, used in our study are both 256×256. The box sizes used for box-counting method are $3, 5, 7, 9, 11$, and 13 pixels in this program. In order to obtain good results, the test-image size must be twice the largest box size in the box-counting method. Since the largest box size is 13×13 pixels, the maximum size that each of the images can be divided into is 32×32 pixels. Thus, we divide our test images into 8×8 pieces maximum. We also test the developed algorithms using 4×4, and 2×2 divisions for comparison purposes.

3.2.1. The PTBC algorithm

The algorithm for PTBC is shown in Fig. 3. As shown, the next step followed by the image division is intensity thresholding at different intensity range bins. The histogram of grayscale pixel intensities may be used to identify the logical threshold period values, such as 32, 64, or 128. Since the BC method is inherently suitable for one-dimensional FD estimation, the intensity values in an image are not appropriately handled in a regular box-counting algorithm. Thus, it is necessary to divide the image intensity into different histogram bins for each of the subimages in addition to dividing the images into subimages. Subsequently, by using the box-counting algorithm, we obtain the FD for each subimage at different intensity bins. We then obtain the cumulative histogram of intensity bins for each of the subimages. The final step is to plot an FD versus a cumulative histogram for each divided subimage of the test and normal images.

3.2.2. The PMBC and PTPSA algorithms

The algorithms for the PMBC and PTPSA methods are shown in Fig. 4. Since the PMBC and PTPSA methods treat intensity as the third dimension, it is not necessary to threshold the intensity in these two methods. After we first load the MR image, we can calculate the image FD either for whole image or for the divided subimages. (However, as described earlier, our PMBC and PTPSA algorithms are more sensitive if the image is divided into subimages. This is due to the fact that the tumor only occupies a few pixels in the whole MR image.) We then compare the FD for the normal MR image to that of the tumor MR image for each subimage to detect a tumor. Thus, we may identify the tumor and its position in the divided image by using either the PMBC or PTPSA method.

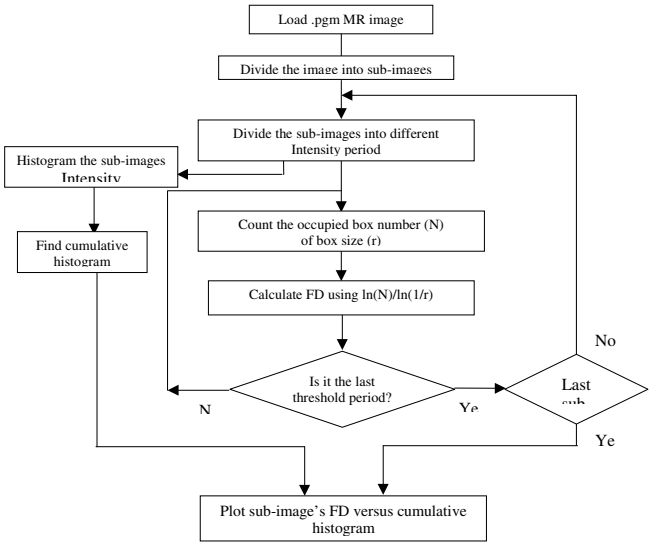

Fig. 3. The PTBC algorithm

4. Results and discussion

In this section we describe the performance of the developed algorithms, which are applied to two different types of images.

4.1. Cloud images

The first type of image is the cloud images with known fractal dimensions that are downloaded from http://www.edv.agrar.tu-muenchen.de/dvs/idolon/idolonhtml /artfrac.html. The images are Brownian surface and are generated with different seed of a random number generator and known fractal dimension. The cloud images are shown in Fig. 5a, 5b, and 5c with known FDs of 2.3, 2.5, and 2.8, respectively. The simple BC algorithm, when applied to the one-dimensional images, such as a Koch curve, provides satisfactory results. However, when the same method is applied to the two- and three-dimensional images, such as the cloud image, the results are unsatisfactory. The average calculated FD using a BC algorithm for all three cloud images in Fig. 5 are obtained as 2.034. The FD results for the cases, even when the images are divided into 4×4 or 8×8 subimages, are all 2.079. Thus, the BC algorithm is not suitable for identifying the differences of two- and higher-dimensional images. The average FD for these three cloud images using the PTBC, PMBC, and PTPSA algorithms, respectively, are shown in

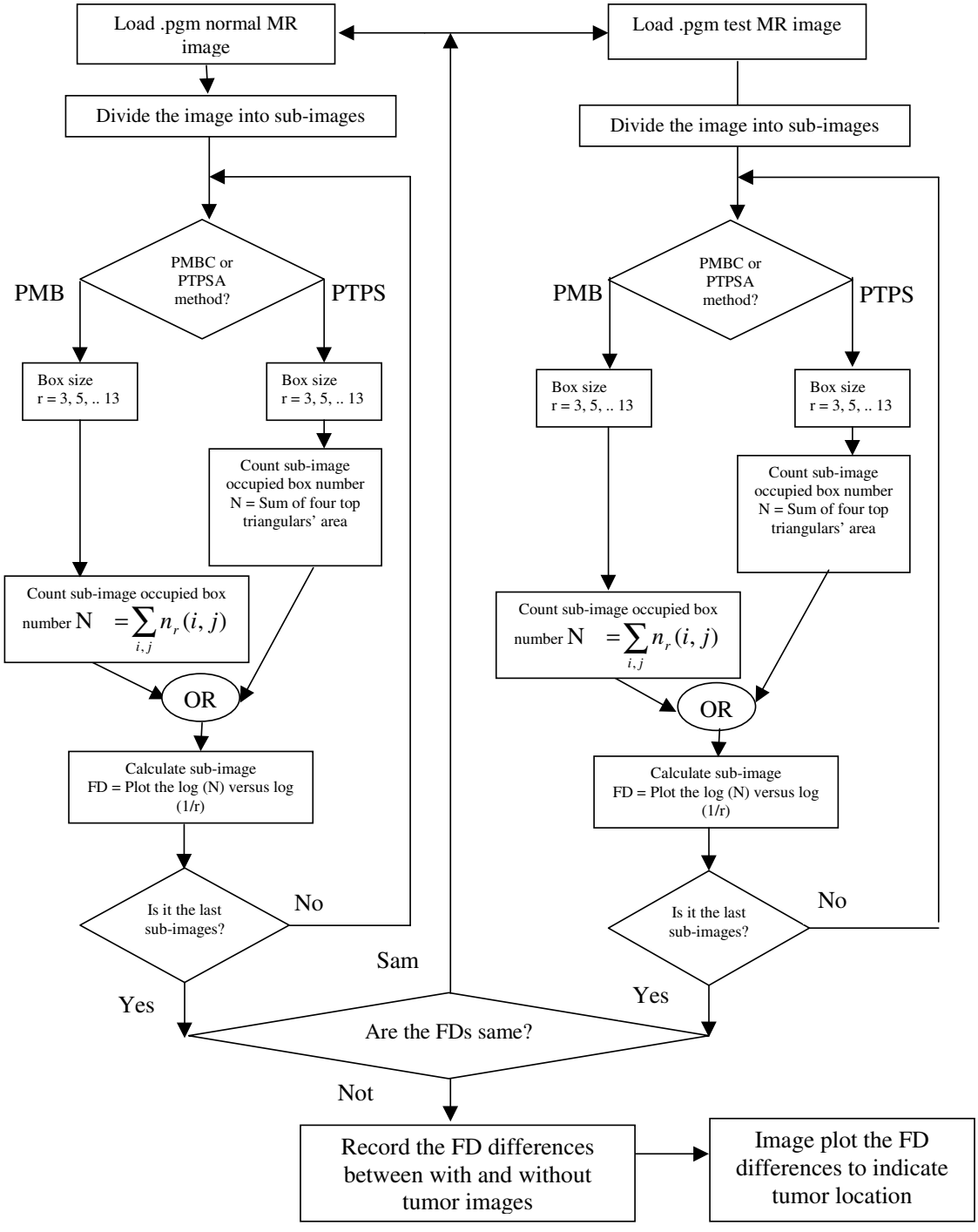

Fig. 4. PMBC (*left*) and PTPSA (*right*) algorithms

Table 1. Table 2 shows the error in average FD calculations for PTBC, PMBC, and PTPSA methods, respectively. From the results in Tables 1 and 2, we infer that the PMBC and PTPSA methods may be more suitable for further estimating three-dimensional FD of rugged surfaces, such as clouds and brain MR images.

4.2. MR brain-tumor image

The second type of image consists of two groups of MR images. The first group of the brain MR images are downloaded from the website http://www.med.harvard.edu/AANLIB. Three normal brain MR images are selected as the reference images, as shown in the first row of Fig. 6a. Since we do not have access to MR images with a progressive history of the patient's tumors, two types of tumor are extracted from tumor MRI and embedded into the normal images. These type-1 and type-2 tumor images are also shown in the second and third rows of Fig. 6a. Thus, the images in Fig. 6a provide us with a synthetic reference for preliminary testing of our PTBC, PMBC, and PTPSA algorithms to detect a tumor in the brain. The second group of MR images is obtained from a tutorial

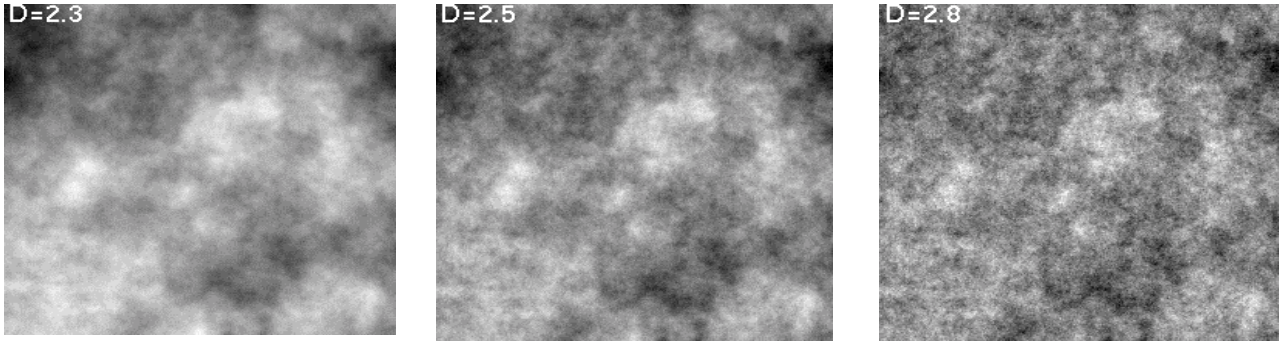

a **b** **c**

Fig. 5a–c. Three cloud image examples with known FD of 2.3, 2.5, and 2.8, respectively

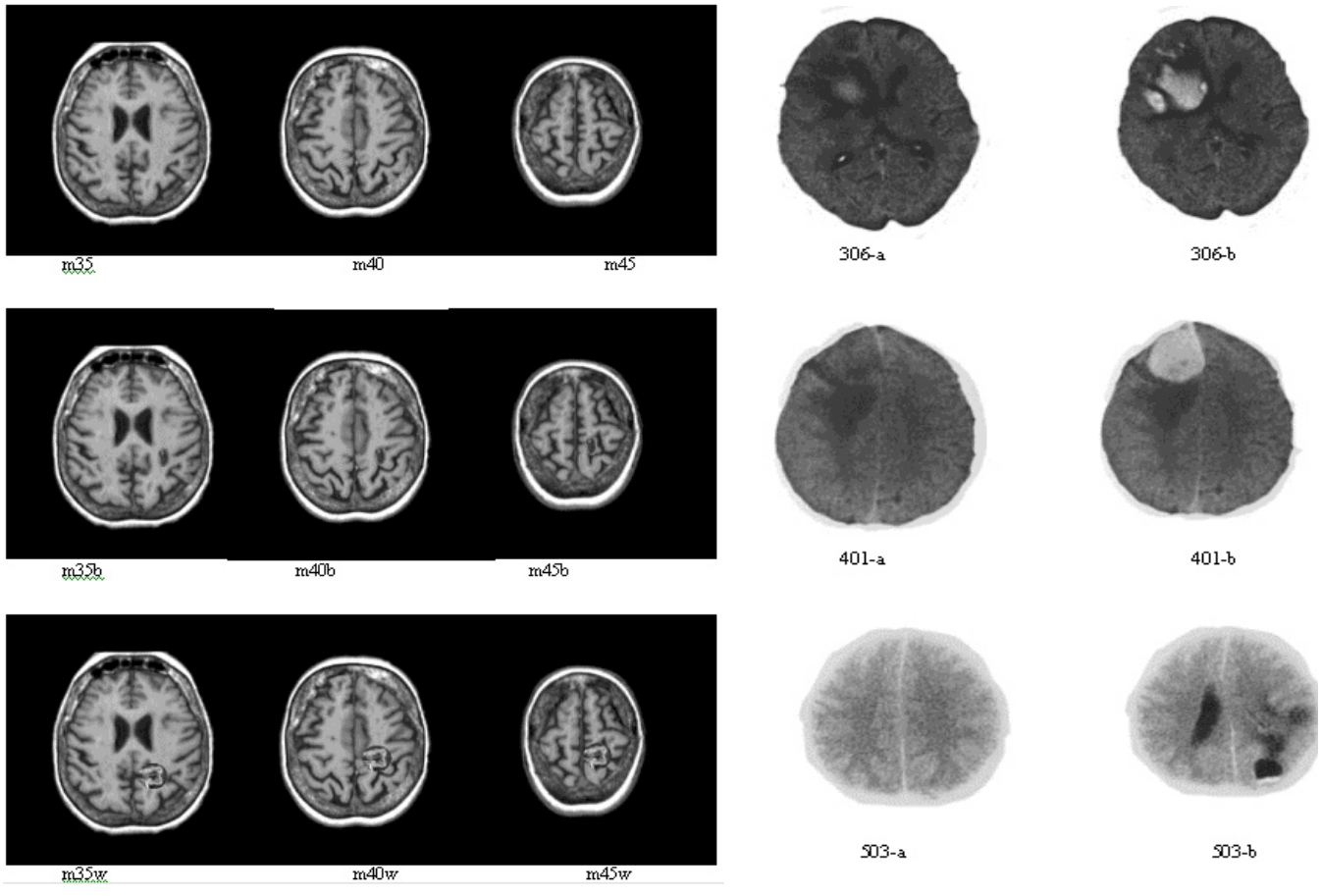

a **b**

Fig. 6. a Embedded tumor MR images: normal. (*First row*) m35, m40, and m45, with type-1 tumor; (*second row*) m35b, m40b, and m45b, with type-2 tumor; (*third row*) m35w, m40w, and m45w; **b** The real tumor MR images selected from ACR; (*first column*) without tumor; (*second column*) with tumor

CD of the American College of Radiology (ACR) real ACR brain MR images that contains intrinsic tumors in patients, as shown in Fig. 6b. The MR images with and without tumors are shown in the first and second columns, respectively, of Fig. 6b. The images in Fig. 6b offer us realistic verification of the tumor-detection performance of our algorithms.

MR image with embedded tumor

We apply our developed algorithms on the first group of MR images in Fig. 6a. We test the images with different combinations of subimage sizes, such as $2 \times 2, 4 \times 4$, and 8×8 and the pixel intensity threshold values of 128, 64, and 32. Our preliminary test results with PTBC algorithms show that the combination of threshold value 32 and subimage size 2×2 offers a recognizable difference between the images with tumor in Fig. 7a and without tumor in Fig. 7b and c, respectively. The cumulative histogram versus FD plots of the normal and tumor images show subtle differences in position $(1, 1)$. This indicates that there are changes between the original and test MR images in the fourth quadrant. However, the PTBC algorithm only identifies the possible image quadrant(s) wherein a

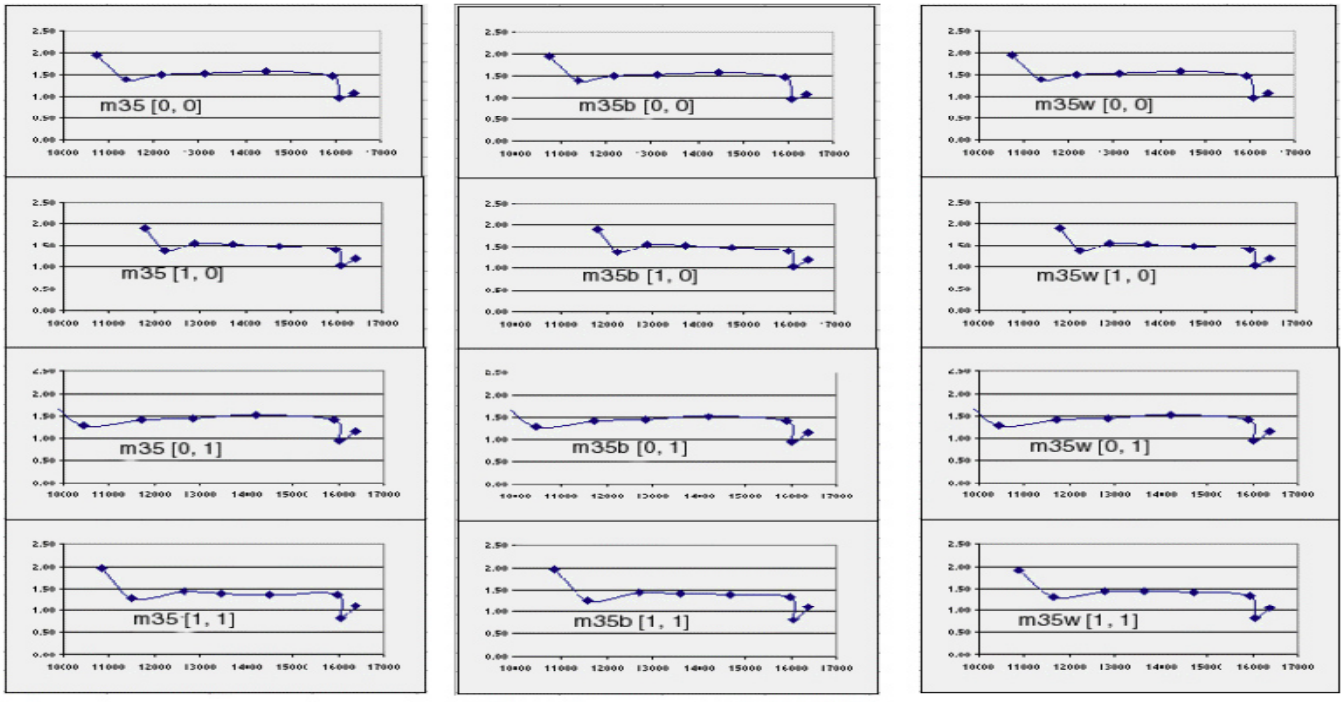

a **b** **c**

Fig. 7a–c. Comparison of FD versus cumulative histogram using PTBC algorithm for MRI without tumor (m35) and type-1 tumor (m35b) and type-2 tumor (m35w), respectively

possible tumor may exist. We are still unable to locate the exact position of the tumor within the quadrant(s). Additionally, the changes in FD for each threshold period are not significantly different, since the changes vary only less than 2% for the cumulative histogram and less than 6% for the FD, respectively. Thus, the PTBC method may be improved further.

Since the PMBC and PTPSA algorithms consider the pixel intensity as the height above a plane, the intensity surface of MR images can be viewed as a rugged surface. It is not necessary to threshold the grayscale value in the PMBC and PTPSA algorithms. We first compare the difference in FD for the subimages divided into 4×4 and 8×8 pieces, respectively.

Table 1. The estimation of average fractal dimensions of cloud images in Fig. 5

Fractal methods	Cloud image #1 $D = 2.3$	Cloud image #2 $D = 2.5$	Cloud image #3 $D = 2.8$
PTBC	2.079	2.079	2.079
PMBC	2.45	2.56	2.70
PTPSA	2.63	2.88	3.11

Table 2. The estimation of the percent error in average fractal dimension for cloud images in Fig. 5

Fractal methods	Cloud image #1 % Error	Cloud image #2 % Error	Cloud image #3 % Error
PTBC	9.6	16.84	25.75
PMBC	6.5	2.4	−3.6
PTPSA	14.4	15.2	11.1

The FD differences between normal and tumor images range between 0–0.06 and 0.04–0.457 for different 4×4 and 8×8 subimages, respectively. Further, some of the test images fail to show the presence of a tumor due to an insufficient number of image subdivisions. Thus, a larger number of image subdivisions is desirable to locate the smaller tumors accurately. A comparison between the PMBC and PTPSA algorithms is shown in Fig. 8. The range of the FD differences in tumor pixels using PMBC is 0.017–0.314, while those using PTPSA lie between 0.012–0.10. In Fig. 8a, the first column shows type-1 tumor images, the second column shows the FD difference between the reference images (as shown in the first row of Fig. 6a) and the type-1 tumor images using PMBC. The fourth column shows type-2 tumor images, and the third column shows FD difference between the reference images and the type-2 tumor images using PMBC. Figure 8b shows the same sequences using PTPSA. We conclude that the PMBC performs better than the PTPSA in detecting embedded tumors in MR brain images.

MR image with realistic tumor

Figure 9 shows plots of a cumulative histogram versus an FD for real ACR brain-MR images that contain intrinsic tumors in patients. In Fig. 9, comparison of corresponding position plots reveals that there is difference between 306-a and 306-b images at location $(0, 0)$. The plots for the other locations such as $(0, 1), (1, 0)$, and $(1, 1)$, however, do not show any such difference. This difference suggests that there may be a tumor at image quadrant $(0, 0)$ of 306-a or 306-b image. From Fig. 9, the other two image pairs, such as 401-a and 401-b and 503a and 503-b, do not show such reliable differences in the corresponding cumulative histogram plots. Fig. 10 shows the differences in FDs for the without and with tumor MR image pairs in

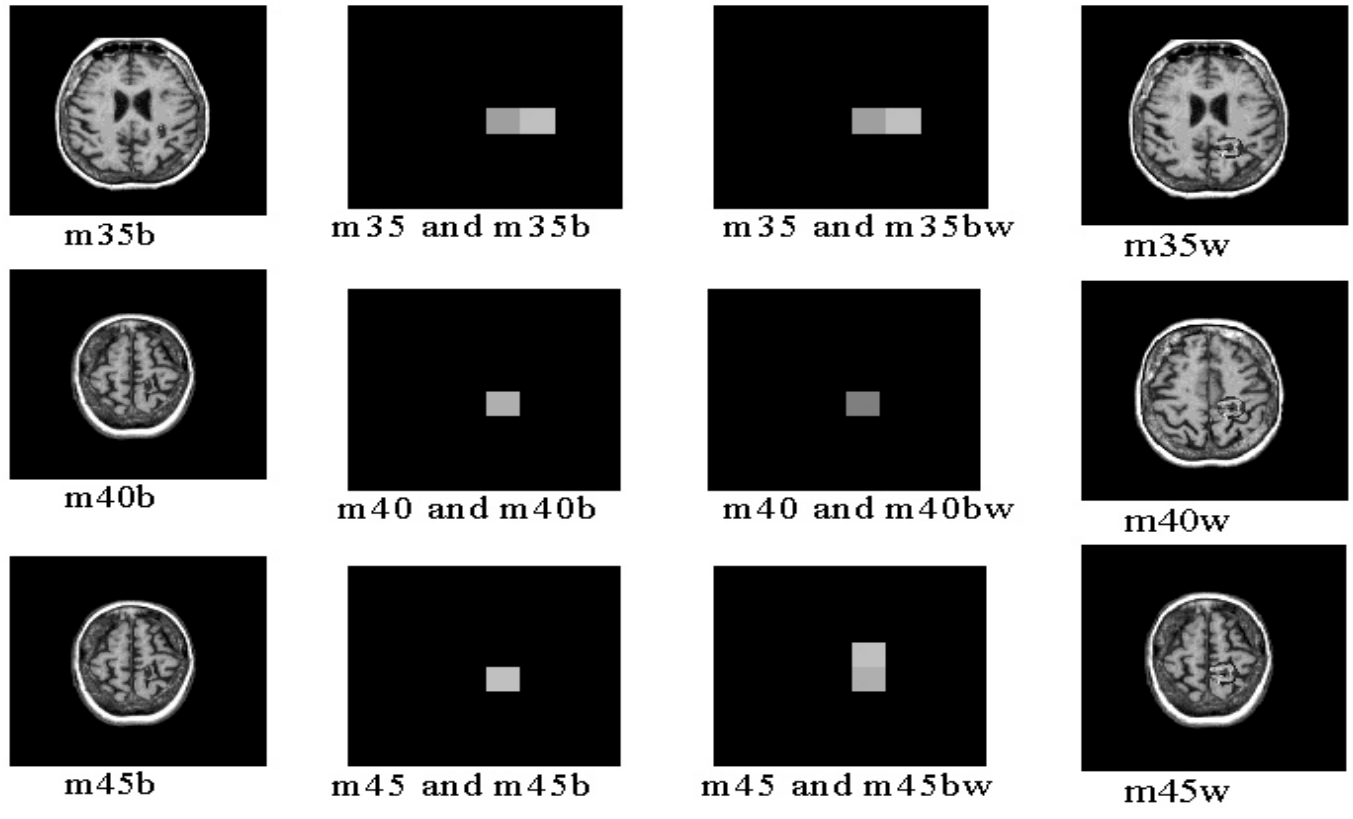

a

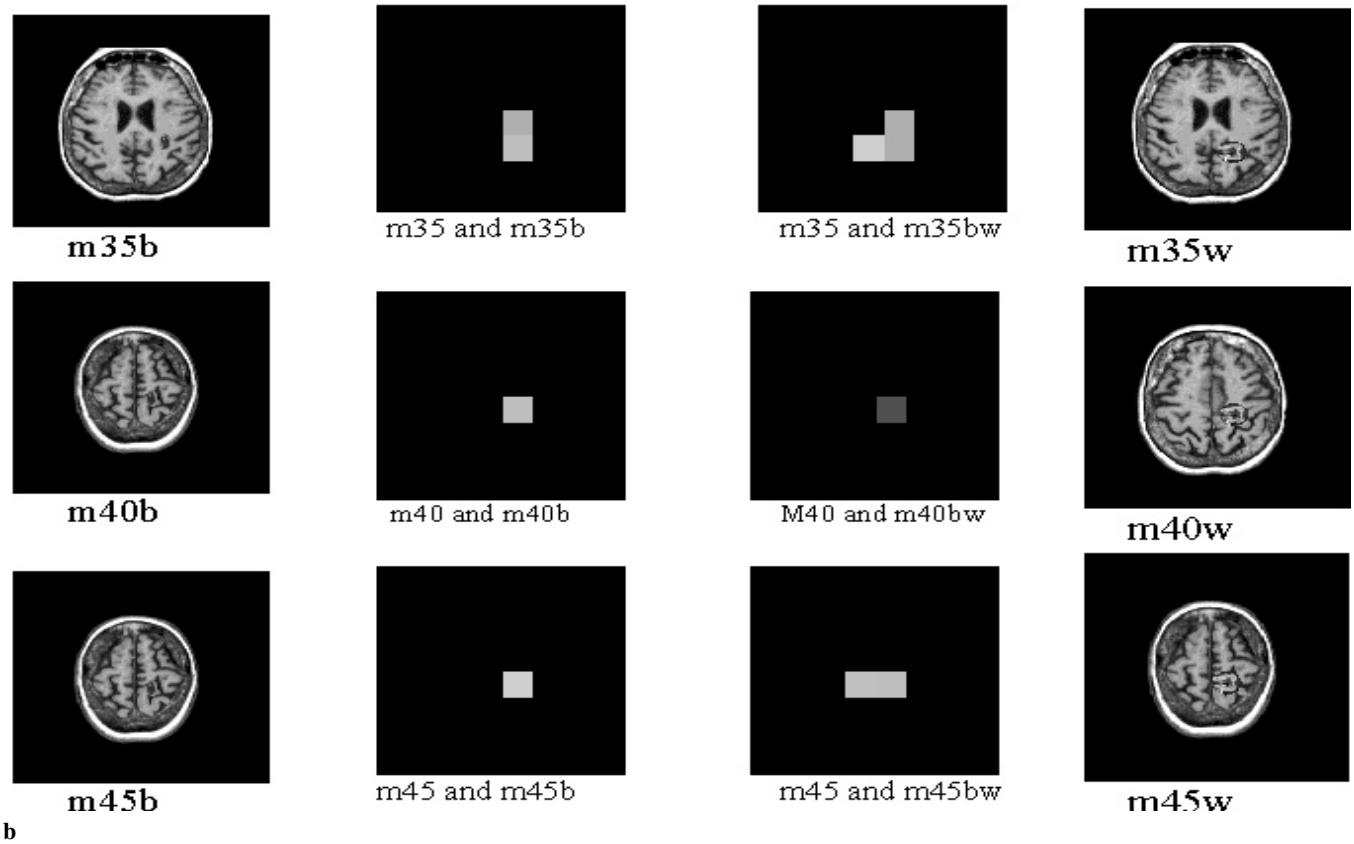

b

Fig. 8. MR images using **a** PMBC and **b** PTPSA algorithms. FD differences indicating tumor locations (*second column*) between the normal (m35, m40, and m45) and type-1 tumor (m35b, m40b, and m45b) and (*third column*) between the normal (m35, m40, and m45) and type-2 tumor (m35w, m40w, and m45w)

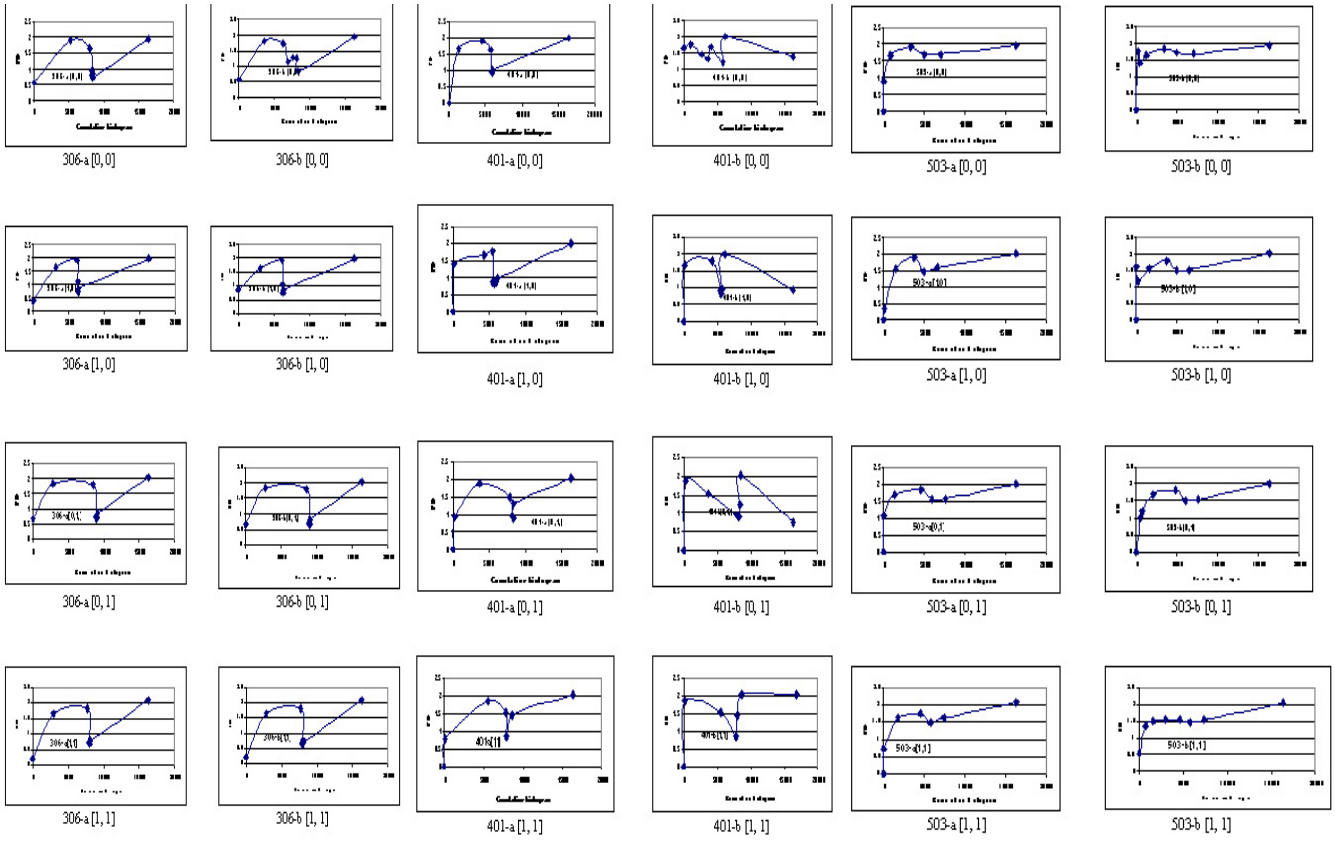

Fig. 9a–c. Comparison of cumulative histogram versus FD for ACR brain MR images: **a** without (306-a) and with (306-b) tumor; **b** without (401-a) and with (401-b) tumor; **c** without (503-a) and with (503-b) tumor

Fig. 6b, such as 306-a and 306-b, 401-a and 401-b, and 503-a and 503-b using the PMBC and PTPSA algorithms, respectively. The differences in the FDs in Fig. 10 clearly show the corresponding tumor locations. Thus, the PMBC and PTPSA methods allow us to detect and locate the tumor in the ACR-CD brain-MR-image data sets considered in this work.

5. Conclusion and future work

In this study, we discuss existing fractal-based algorithms and propose three novel improvements of these algorithms for identifying tumors in brain MR images. We use the BC algorithm, the widely accepted estimation method, as the basis for developing PTBC, PMBC, and PTPSA algorithms, respectively. We employ the cumulative histogram versus FD with different threshold values for the PTBC method. A piecewise FD computation is exploited for the PTBC and PTPSA methods, respectively. The BC method for the FD estimation of a one-dimensional signal offers good results, as expected. However, it is not amenable to the rough surface images with two or higher dimensions, such as clouds and MR images. The PTBC method can detect the tumor in MR images, though it is hard to locate the exact position of the tumor. Further, the changes in FD at each threshold value are not significant. Both PMBC and PTPSA methods detect and locate the tumor based on tumor FD differences in embedded-tumor MR images as well as ACR-CD real brain-tumor MR images. Thus, the embedded-tumor MR images offer good preliminary testing of our algorithms, while the ACR tutorial CD results show the validity of our algorithm in an example test case.

Comparing the PMBC and PTPSA methods, the PMBC algorithm is more sensitive and offers better results in detecting and locating the tumor. Note that the piecewise division of images still preserves the fractal nature of the tumors for all three methods. However, the cumulative histogram formulation in PTBC may contribute to non-fractal handling of the MR images and, hence, unsatisfactory performance of the method. Further, our algorithms are applied to the 8-bit quantized brain MR images in ACR CD. Application of our algorithms to 12-bit quantized MR images may offer better tumor detection due to improved image resolution and fractal information.

In the future, we need to improve the fractal-based tumor detection algorithms to test brain MR images with progressive tumor-development information. Some of the future works may include development of an FD database that contains continuous sections of normal brain MR images. A patient may be diagnosed with a possible brain tumor if the corresponding brain MR image's FD differs from that of reference image sections in the database. However, it may be challenging to record the brain MR images at exactly the same positions at different times. Further, the requirement of normal brain images as references for our proposed algorithms needs to be alleviated.

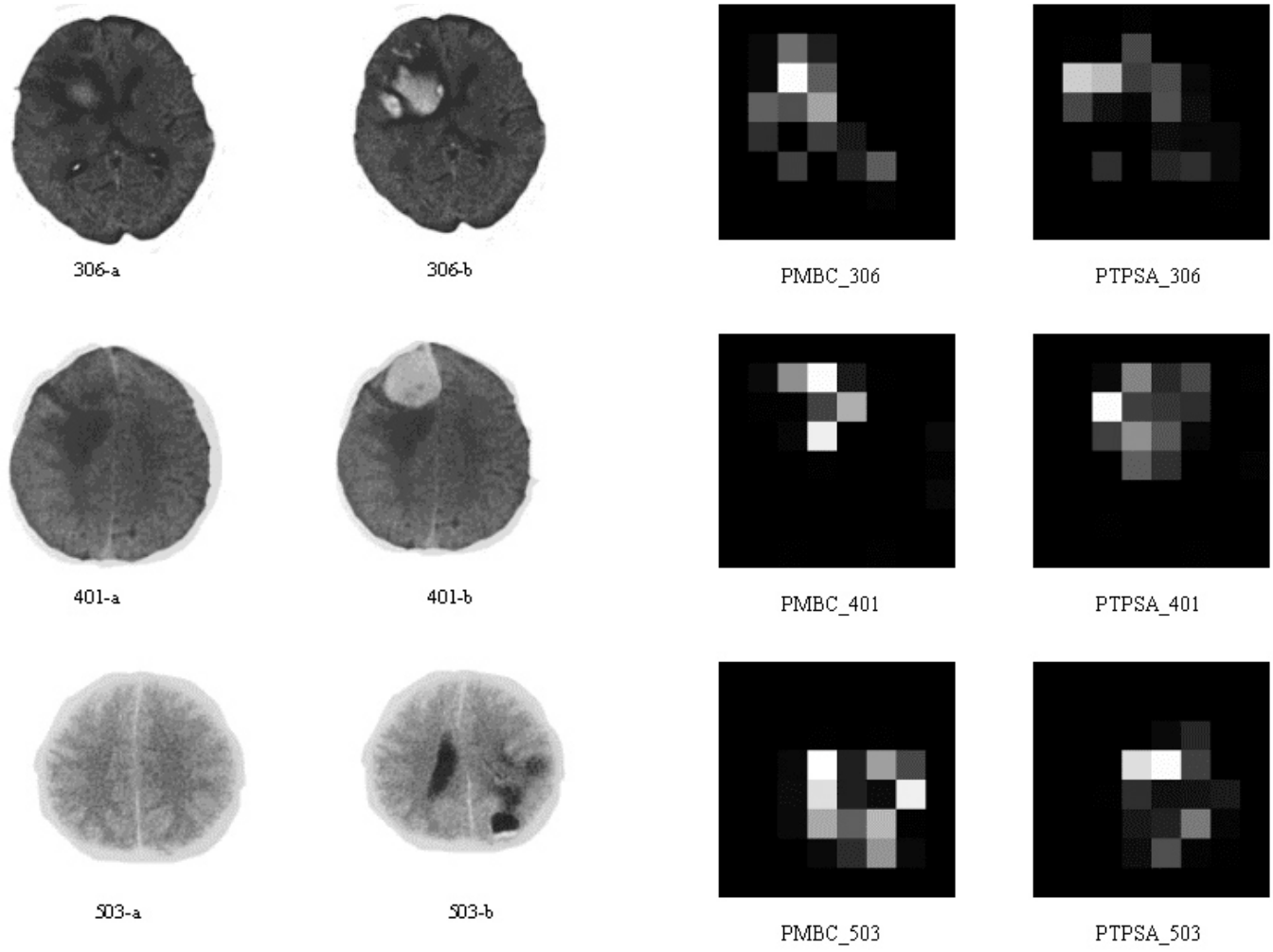

Fig. 10. FD differences indicating tumor locations using ACR MR brain images: **a** images without tumor; **b** images with tumor; **c** FD difference between *first* and *second* columns using PMBC; and **d** FD difference between *first* and *second* columns using PTPSA

Acknowledgements. Wei Jia wishes to thank ND EPSCoR for partial support of this research through a biomedical SEED Grant. The authors would also like to thank anonymous reviewers for constructive comments.

References

1. Mandelbrot BB (1983) The fractal geometry of nature. Freeman, San Francisco
2. Comis D (1998) Fractals–A bridge to the future for soil science. Agr Res Mag 46(4):10–13
3. Sarkar N, Chaudhuri BB (1992) An efficient approach to estimate fractal dimension of textural images. Pattern Recogn 23(9):1035–1041
4. Davies S, Hall P (1999) Fractal analysis of surface roughness by using spatial data. J Roy Stat Soc, B Stat Method 61(1):3–29
5. Chen J, Zheng B, Chang YS, Shaw CC, Towers JD (1994) Fractal analysis of trabecular patterns in projection radiographs. An assessment. Investig Radiol 29(6):624–629
6. Osman D, Newitt D, Gies A, Budinger T, Truong V, Majumdar S (1998) Fractal based image analysis of human trabecular bone using the box counting algorithm: impact of resolution and relationship to standard measures of trabecular bone structure. Fractal 6(3):275–283
7. Caldwell CB , Stapleton SJ, Hodsworth DW, Jong RA, Weiser WJ, Cooke G, Yaffe MJ (1990) Characterisation of mammographic parenchymal pattern by fractal dimension. Phys Med Biol 35(2):235–247
8. Webber RL, Underhill TE, Horton RA, Dixon RL, Pope TL Jr (1993) Predicting osseous changes in ankle fractures. IEEE Eng Med Biol Mag 12(1):103–110
9. Mihara N, Kuriyama K, Kido S, Kuroda C, Johkoh T, Naito H, Nakamura H (1998) The usefulness of fractal geometry for the diagnosis of small peripheral lung tumors. Nippon Igaku Hoshasen Gakkai Zasshi 58(4):148–151
10. Pohlman S, Powell KA, Obuchowski NA, Chilcote WA, Grundfest–Broniatowski S. (1996) Quantitative classification of breast tumor in digitized mammograms. Med Phys 23(8):1337–1345
11. Swarnakar V, Acharya RS, Sibata C, Shin K, Fractal based characterization of structural changes in biomedical images. SPIE 2709:444–455
12. Bru A, Pastor JM, Fernaud I, Bru I, Melle S, Berenguer S (1998) Super-rough dynamics on tumor growth. Phys Rev Lett 81(18):4008–4011
13. Penn AI, Thompson SF, Schnall SF, Loew MH, Bolinger L (2000) Fractal discrimination of MRI breast masses using multiple segmentations. In: Hanson KM (ed) Medical imaging 2000: Image processing. SPIE 3979: 959–966

14. Falconer KJ (1990) Hausdorff measure and dimension. In: Fractal geometry mathematical foundations and applications. John Wiley, Cambridge
15. Clarke KC (1986) Computation of the fractal dimension of topographic surfaces using the triangular-prism-surface-area method. Comput Geosci 12(5):713–722
16. Mandelbrot BB, Van Ness JW (1968) Fractional Brownian motions, fractional noises and applications. SIAM Rev 10(40):422–437

Khan M. Iftekharuddin is an assistant professor at the department of Electrical and Computer Engineering at the University of Memphis (U of M). Prior to the U of M, he was on the faculty of the department of Computer Science and Electrical and Computer Engineering at North Dakota State University (NDSU) for two years. He obtained his B.Sc. degree from Bangladesh Institute of Technology in 1989. He received an M.S. and a Ph.D. both in electrical engineering from the University of Dayton in 1991 and 1995, respectively. His research interests include sensor signal acquisition and modeling; digital, optical, and multimedia signal and image processing; embedded systems; optical computing and interconnection; applications of artificial-neural inference techniques; automatic target recognition (ATR); and biologically-inspired ATR. He has published more than 60 refereed journal papers and conference proceedings. He was named the researcher of the year in the college of Engineering and Architecture at NDSU for 2000.

Wei Jia graduated from the North Dakota State University with an M.S. in computer science in 2000. He is currently working with Indentix Corporation in Minneapolis, Minn.

Ronald Marsh received a B.S. degree in physics from North Dakota State University in 1985 and M.S. and Ph.D. degrees in computer science from North Dakota State University in 1985 and 1998, respectively. He was an optical engineer at the Naval Air Warfare Center at China Lake, Calif. from 1985 through 1991, where he developed camera systems and optical correlation systems. He joined the Computer Science faculty of North Dakota State University in 1998. In 1999 he joined the Computer Science faculty of the University of North Dakota. He is currently an assistant professor of Computer Science and the Graduate Director of Computer Science. His research interests include image processing and pattern recognition.